Supplementary Information to "Conformational Changes and Flexibility of DNA Devices Observed by Small-Angle X-Ray Scattering"

Linda K. Bruetzel[†], Thomas Gerling[‡], Steffen M. Sedlak[†], Philipp U. Walker[†], Wenjun Zheng[§], Hendrik Dietz[‡], Jan Lipfert[†,*]

[†]Department of Physics, Nanosystems Initiative Munich, and Center for Nanoscience, LMU Munich, Amalienstrasse 54, 80799 Munich, Germany

[‡]Physik Department, Walter Schottky Institute, Technische Universität München, Am Coulombwall 4a, 85748 Garching near Munich, Germany

[§]Physics Department, State University of New York at Buffalo, Buffalo, New York 14260, United States

[*]Corresponding author: Jan Lipfert; Email: Jan.Lipfert@lmu.de; Phone: +49-89-2180-2005

Supplementary Information consisting of

- **Materials and Methods**
- **Supplementary Table S1**
- **Supplementary Figures S1-S13**
- **Supplementary References**

Materials and Methods

DNA origami assembly and purification

DNA origami objects were designed using caDNAno v.02.[1] Three different variants of the switch object were prepared for the SAXS experiments (Supplementary Figure S1-S3): two static variants that were permanently locked either in the open state (switch O) or the closed state (switch C), and a dynamic variant with 16 activated stacking interactions (switch D) (Figure 1). Each structure contained 16128 nucleotides. The scaffold DNA (p8064) was prepared as previously described.[2] Staple DNA strands were synthesized by solid-phase chemical synthesis (Eurofins Genomics GmbH, Ebersberg, Germany; HPSF purification). DNA origami objects were self-assembled by subjecting the one-pot reaction mixture to a thermal annealing ramp using a thermal cycling device (TETRAD; MJ Research – now Biorad).[3] The reaction mixture contained 50 nM scaffold DNA (p8064), 200 nM of each staple DNA strand, folding buffer (1 mM EDTA, 5 mM TrisBase, 5 mM NaCl; pH 8) and 20 mM $MgCl_2$. After a 15 min-long thermal denaturation step at 65 ˚C, the thermal annealing ramp covered the temperature interval [58 – 55 ˚C] with a rate of 1 ˚C/90 min. Excess staple DNA strands were removed from the reaction mixture by performing two rounds of polyethylene glycol (PEG) precipitation.[4] The resulting pellets were dissolved in folding buffer (1 mM EDTA, 5 mM TrisBase, 5 mM NaCl; pH 8) containing 5 mM $MgCl_2$. To allow for equilibration, all samples were incubated at 40 ˚C and 400 rpm overnight. Residual PEG was removed from the samples by performing three rounds of ultrafiltration (30K Amicon Ultra-0.5mL; Merck Millipore). Filters were equilibrated by adding 500 µl folding buffer containing either 5, 15, or 30 mM $MgCl_2$ at 2000 x *g* and 25 ˚C for 2 minutes. Then, 50 µl sample was mixed with 450 µl folding buffer and centrifuged at 8000 x *g* and 25 ˚C for 15 minutes. The flow-throw was discarded and 480 µl of folding buffer was added to the recovered sample. The concentration of the different samples was determined using a spectrophotometer (NanoDrop 8000; Thermo Scientific). All samples were measured at three different DNA origami object concentrations (25 nM, 50 nM, and 100 nM), prepared by dilution using the appropriate buffers. Samples of the switch O and switch C were measured in folding buffer (1 mM EDTA, 5 mM TrisBase, 5 mM NaCl; pH 8) containing 15 mM $MgCl_2$. Samples of the switch D variant were measured in folding buffer containing either 5 mM or 30 mM $MgCl_2$.

Scaling relationship for the concentration requirements for nucleic acid SAXS measurements

For monodisperse solutions and in the absence of interparticle interference effects, the forward scattering intensity *I(0)* scales linearly with sample concentration *c* and quadratically with the molecular weight *MW*:[5,6]

$$I(0) = K\, c\, (\Delta\rho)^2\, p^2\, (MW)^2 \qquad \text{(S1)}$$

$\Delta\rho$ and p are the average electron contrast and the partial specific volume of the molecule and are approximately constant for all nucleic acid molecules.[6] K is an instrument specific constant, which is typically determined from comparison to a molecular weight standard. Even though Equation 1 only strictly holds for the forward scattering intensity, it provides a rough estimate of the scattering signal expected in a SAXS measurement at a given sample concentration and molecular weight. For the set of samples analyzed in this work (Figure 2a), the concentrations required for good quality SAXS measurements follows roughly the anticipated $\sim MW^{-2}$ relationship (Figure 2a, solid line) from Equation S1. Treating the exponent as a free parameter, i.e. fitting the data to a relationship $\sim MW^{-\nu}$, yields a better fit with $\nu = 1.30$ (Figure 2a, dashed line). A shallower dependence than $\sim MW^{-2}$ on the number of nucleotides can be rationalized by considering the fact that SAXS profiles for nucleic acids are maximal at low q and fall off for higher q. Importantly, the fall off with increasing q is more rapid for larger structures, suggesting that for these structures higher concentrations than suggested by the simple $\sim MW^{-2}$ scaling are required to obtain a decent signal at higher q-values. Our DNA origami measurements at 25 nM (Figure 2a, red star) are in excellent agreement with the extrapolated scaling relationship with $\nu = 1.30$ (Figure 2a, dashed line); including the origami data point into the fit yields a nearly identical scaling exponent of $\nu = 1.36$.

SAXS measurements

SAXS measurements were performed at beamline BM29, ESRF, Grenoble[7] at an X-ray wavelength λ of 0.99 Å, using a sample-to-detector distance of 2.87 m and a Pilatus 1M detector, resulting in a q-range of 0.03 to 5 nm^{-1} ($q = 4\pi\cdot\sin(\theta)/\lambda$, where θ is the total scattering angle). For each sample concentration ten runs with an exposure time of 1 s in 'flow' mode were conducted at room temperature. SAXS data of dynamic switch samples for Mg^{2+} titration experiments were collected at beamline P12 (DESY, Hamburg, Germany[8]) at an X-ray wavelength λ of 1.18 Å and a sample-to-detector distance of 6 m, resulting in a

q-range of 0.03 to 2.2 nm^{-1}. Data were acquired in 'flow' mode with an exposure time of 95 ms and 150 frames per sample at room temperature. For each experiment buffer samples were measured using identical procedures before and after each sample measurement. Sample and buffer data from each run were analyzed for radiation damage; no damage was observed in any of the measurements. Matching sample and buffer profiles were averaged and buffer profiles were subtracted for background correction. Unless otherwise noted the scattering profiles shown in this work correspond to data from averaged and buffer subtracted intensity profiles measured at a DNA origami concentration of 100 nM.

SAXS data analysis

We performed Guinier analyses to obtain radii of gyrations for all measured DNA origami structures, by fitting the logarithm of the scattering intensity as a function of q^2 to a straight line for small values of q.[9] Due to the large size of the DNA origami objects, we extended the fitting range criterion to $q_{max} \cdot R_g < 1.6$,[10] enabling us to obtain reasonable estimates of the forward scattering intensity and radii of gyration that, nonetheless, should still be treated as approximations (Supplementary Figure S5a).

In addition to determining the global R_g of the object from the scattering signal at very low q, DNA origami structures investigated in this work can be approximated as rod-like particles with an axial length L (~95 nm) and a radial cross section A (~20 nm and ~14 nm for switch C and switch O, respectively) (Figure 1). The total scattering intensity is approximated by:[11]

$$I(q) = I(q)_{axial} * I(q)_{cross} = \frac{\pi \cdot L}{q} * A^2 \Delta\rho^2 \exp\left(-\frac{q^2 R_c^2}{2}\right) = \frac{a}{q} \exp\left(-\frac{q^2 R_c^2}{2}\right) \quad \text{(S2)}$$

where the first factor is related only to the axial component and the remaining part corresponds to the cross-sectional scattering with an electron density contrast $\Delta\rho$. The pre-factors can be combined into a single fitting constant a. Equation S2 is valid in the range of $q_{min} = 2\pi/R_g$ and $q_{max} = 2\pi/R_c$, which corresponds to a q-range of ~ 0.2 – 0.9 nm^{-1} (1.3 nm^{-1}) for the switch C (switch O) object. Values for a and R_c were obtained by performing a least squares analysis in the valid q-range (Supplementary Figure S5b,c). The R_c value can be used for calculating the corresponding radius according to $R_c^2 = R^2/2$ when describing the switch object by a cylinder model with R = 10 nm (corresponding to a diagonal D = 20 nm of the cross-sectional area of the closed arm) and R = 7 nm (corresponding to the diagonal $D \approx 14$ nm of the cross-sectional area of the open arm).

Furthermore, we computed the pair distance distribution function $P(r)$ as described by Moore[12] using an indirect Fourier transformation in terms of a sine series expansion, based on the Shannon sampling theorem.[13] The large size of the DNA nanostructure is beneficial in the

context of the series expansion, since the maximum number of series coefficients (a_n) is given by $n_{max} = \frac{q_{max} \cdot D_{max}}{\pi}$, where D_{max} describes the maximum particle dimension. The calculation of *P(r)* requires a fixed value for D_{max}, which we expected to be around 95 nm for the switch object (Figure 1). We tested different values for D_{max} ranging from 60 – 130 nm for all switch samples by calculating a chi-squared value (χ^2), which describes the discrepancy between the experimental data and the fit, for each D_{max}. The χ^2 values decay approximately exponentially with increasing D_{max} (Supplementary Figure S6) until they plateau for $D_{max} > 90$ nm. For D_{max} values > 95 nm no change in the overall shape of the *P(r)* was observable, thus a D_{max} of 95 nm was taken as the best estimate of D_{max}. *P(r)* functions shown were normalized to give equal surface areas.

Structural parameters described above as well as the two-state model fitting (see main text) were calculated from scattering profiles averaged from 10 independent runs for all three sample concentrations. The related errors represent the standard deviation.

Computing SAXS profiles from atomic models of DNA origamis

We generated atomistic models for the open and closed switch object with the CanDo software assuming idealized DNA helix and junction geometries.[14] CanDo simulations were run using the CanDo webserver (http://cando-dna-origami.org); computation time was dependent on the load of the server and the design of the structure, but typically in the range of hours. There are several methods to predict a scattering profile from an atomistic model that differ in various aspects of the computation. We used the programs *CRYSOL*[15] and *FOXS*[16] for calculation of the theoretical scattering curves from atomistic models. *CRYSOL*[15] computes the scattering intensity using a spherical harmonics expansion and scattering contributions from the hydration shell around the molecule are taken into account by assuming a homogenous 3 Å thick border layer with a default density contrast value of 0.03 e/Å^3. The program *FOXS*[16] evaluates the theoretical scattering profile from the Debye formula and the particle hydration layer is modeled as a function of surface accessibility.[17] As a complementary and more simplistic approach, we utilized a custom written routine in C, adapted from the program SAXS3D,[18] to determine theoretical scattering profiles based on a coarse-grained representation of the switch objects including only scattering centers per DNA base. For the Debye formula routine, only one particle (placed at the phosphorus position) per base was used and the *q*-range was set to 0 - 3 nm^{-1} including 300 datapoints. *CRYSOL* was run in interactive mode, setting the order of harmonics to the maximum value of 50, given the large size of the switch object. The number of points in the theoretical curve was fixed to 800

within a q-range from 0 - 3 nm^{-1}; the remaining parameters were set to default values, without fitting the theoretical curve to the experimental data. *FOXS* was executed in default mode using the same number of points and q-range as applied in *CRYSOL*. Calculated scattering profiles were fitted to the experimental data of the switch C and switch O sample by performing a linear fit including a constant offset (Figure 5a,b and Supplementary Figure S9). To test the influence of the ion shell surrounding the switch object on the shape of the theoretical scattering profiles we investigated solvent density values ranging from 0.334 e/$Å^3$ (default, corresponding to the solvent density of water) and 0.344 e/$Å^3$ in *CRYSOL* (Supplementary Figure S12) and from 0.307 e/$Å^3$ (minimum) – 0.388 e/$Å^3$ (maximum) in *FOXS* (data not shown). In addition, we varied the contrast of the solvation shell surrounding the DNA origami; i.e. we varied the difference in electron density between the hydration layer and bulk solution, testing values from 0.06 to 0.25 e/$Å^3$ (0.03 e/$Å^3$ is the default value) in *CRYSOL*. The latter is based on a literature value reported for experiments on Mg^{2+} ions dissolved in water.[19] Increasing the contrast or solvent density to even higher numbers would not correspond to physically plausible solution conditions.

Electrostatic potential calculations and estimates of the ion atmosphere

To estimate the extent of the ion atmosphere around the DNA origami objects used in this work, in particular in comparison to simple double-stranded DNA molecules for which the role of ion scattering has been investigated in detail previously,[20-23] we performed simple electrostatic calculations. We calculated the electrostatic potential with a custom-written MATLAB script based on the Debye-Hückel/Poisson-Boltzmann approximation and on the atomistic model of a 35 bp DNA and the switch C, including only the positions of the phosphate atoms of the DNA backbone. Each phosphate atom was described by its position (x_i,y_i,z_i) and modeled as a negatively charged point charge. Moreover, we assumed a Debye-Hückel exponential screening factor to account for the ionic screening due to mobile, dissolved ions. The resulting screened electrostatic potential at a certain position r_i is given by the sum of the electrostatic potential over all phosphate atoms:

$$\Phi(r)_{screen} = \sum_i \frac{-q}{4\pi\varepsilon_0\varepsilon_r r_i} \exp\left(\frac{-r_i}{\lambda_D}\right) \quad \text{(S3)}$$

with the charge of q = 1.602 x 10^{-19} C the vacuum permittivity ε_0 = 8.85 x 10^{-12} F m^{-1}, the relative permittivity of water ε_r = 80.4 and a Debye length λ_D= 9.9 Å corresponding to the high-salt experimental buffer condition for the switch object consisting of 5 mM NaCl and

30 mM $MgCl_2$. We calculated the corresponding ion concentrations around the 35 bp DNA and the switch C assuming the Boltzmann distribution:

$$c^{\pm} = c_0^{\pm} \exp\left(\frac{-q\,\Phi(r)_{screen}}{k\,T}\right) \quad \text{(S4)}$$

where c_0 correspond to the initial ion concentration , kT = 4.11x 10^{-21} J and $\Phi(r)_{screen}$ was computed by Equation S3.

Normal mode refinement of models against SAXS data

To refine the initial model against the experimental SAXS data, we employed a flexible fitting method based on a coarse-grained (one-bead-per-residue) nucleic acid representation and a modified elastic network model that allows large-scale conformational changes while maintaining pseudobonds and secondary structures.[24] This method optimizes a pseudoenergy that combines the modified elastic network model energy with a SAXS-fitting score and a collision energy that penalizes steric collisions. The optimization process effectively uses a weighted combination of normal modes to iteratively improve the fitting of SAXS data. To apply this method to a large DNA object, the following modifications and improvements have been made to the methods described previously.[24] First, each DNA nucleotide is represented by a bead located at the C4' atomic position. All pairs of DNA beads within a cutoff distance of 35 Å are linked to build an elastic network model (see Equation 1 of Ref.[24]). The coarse-grained form factors for DNA nucleotides are taken from the Fast-SAXS-Pro program.[25] Second, to stabilize the local structure of double-stranded DNA, for nucleotide i and i' that form a base pair, additional springs are added between the following pairs: (i, i'), (i±1, i'), (i, i'±1), (i-1, i+1), (i'-1, i'+1). Third, the SAXS fitting score (Equation 10 of Ref.[24]) is modified to the following:

$$E_{SAXS} = f_{SAXS} \cdot N \cdot \mathrm{X}^2 \quad \text{(S5)}$$

with a chi-squared of:

$$\mathrm{X}^2 = \min_c \left\{ \sum_i \frac{[c \cdot I_m(q_i) - I_t(q_i)]^2}{\sigma_i^2} \Big/ \sum_i \frac{[I_t(q_i)]^2}{\sigma_i^2} \right\} \quad \text{(S6)}$$

The constant pre-factor f_{SAXS} = 30, N is the number of DNA beads and q_i is the scattering vector uniformly sampled between 0 and 3 nm^{-1} with an increment of 0.025 nm^{-1}, I_m is the model SAXS profile, I_t is the target SAXS profile measured experimentally, and σ is the experimental error of I_t. Fourth, no hydration shell is modeled, which is expected to have negligible effect on SAXS fitting especially for large molecular systems.[17] Fifth, to reduce memory usage for the large systems, all Hessian matrices except H_{SAXS} in Equation 11 of

Ref.[24] are stored in the sparse matrix format, and the H_{SAXS} term is omitted. The linear equation in Equation 11 of Ref.[24] is solved using the CHOLMOD suite (http://www.cise.ufl.edu/research/sparse). Normal mode refinement calculations were run on an Intel Xeon Processor L5520 (8M Cache, 2.26 GHz); the full refinement of a structure using 209 *q*-values required 120 h of computational time.

Ensemble FRET measurements via donor quenching

Ensemble FRET experiments in solution on DNA origami switch objects were conducted and analyzed as described in the supplementary information of Gerling *et al*.[26] Fluorescently labeled switch particles exhibit low and high FRET signals upon a conformational change from the open to the closed state, respectively. In order to dissect the populations of the closed and open conformation of the switch D sample as a function of $MgCl_2$ concentration, ensemble FRET measurements were performed on switch C, switch O and switch D samples while titrating $MgCl_2$ concentrations in the range of 5 mM to 25 mM (Supplementary Figure S7), as published previously.[26] Ensemble FRET data of the switch C and switch O sample serve as reference samples for the closed and open state, respectively.

To compare the fractions of populations derived from ensemble FRET experiments to the fractions obtained from the two-state model for the switch D sample of the SAXS data, each titration curve was fitted up to a $MgCl_2$ concentration range of 30 mM, assuming a two-state model where the resulting ensemble FRET value (E_{FRET}) is given by:

$$E_{FRET} = f_c \cdot E_c + f_o \cdot E_o \tag{S7}$$

E_c and E_o correspond to ensemble FRET values and the coefficients f_c and f_o are fractional occupancies of the closed and open state, respectively. From statistical thermodynamics of a two-state system it follows that $f_c + f_o = 1$ where f_c is calculated as follows:

$$f_c = \frac{1}{1+\exp\left(-\frac{\Delta G}{kT}\right)} \tag{S8}$$

The overall free energy difference between the open and closed state $\Delta G(MgCl_2)$ is given by:

$$\Delta G(MgCl_2) = \Delta G_0 + m_c \cdot c(MgCl_2) \tag{S9}$$

where ΔG_0 is the free energy difference at a reference $MgCl_2$ concentration of 5 mM, and m_c represents the cation sensitivity parameter. We obtained a ΔG_0 = 1.5 kcal/mol and m_c = -0.4 kcal/(mol mM) from a least-square fitting of the experimental data.

Values from the fitted titration curves at low (5 mM) and high (30 mM) $MgCl_2$ concentrations were used to determine the fraction of closed switch D particles. Analogous to the two-state model approach applied on the SAXS data, the ensemble FRET value of the switch D sample (E_d) can be described by a linear superposition of the open and closed states represented by ensemble FRET values of switch O (E_{so}) and switch C (E_{sc}), respectively:

$$E_d(\mathrm{MgCl_2}) = f_c \cdot E_{sc}(\mathrm{MgCl_2}) + f_o \cdot E_{so}(\mathrm{MgCl_2}) \quad \text{(S10)}$$

For the evaluation of the conformational state of the switch D sample at low and high $MgCl_2$ concentrations, we averaged fitted ensemble FRET values for each sample taking values at the exact concentration (e.g. E_d(5 mM)) and the values of the precedent and subsequent concentration (i.e. E_d(4 mM) and E_d(6 mM)). Based on these values a least squares fit was performed to determine the closed fraction of the switch D sample at high (30 mM) and low (5 mM) $MgCl_2$ concentrations (Figure 4d). Errors were calculated based on a propagation of uncertainty.

Supplementary Table

Supplementary Table S1. Comparison of the radius of gyration (R_g) and the cross-sectional R_g (R_c) determined from the theoretical scattering profiles calculated with *CRYSOL, FOXS* and a custom written *C* script for the static switch samples. For Guinier analysis the fitting range $q_{max}R_g < 1.3$ was used and for R_c calculations a q-range of ~ 0.2 – 0.9 nm^{-1} (1.3 nm^{-1}) for the switch C (switch O) object was defined.

Sample	R_g (nm)	R_c (nm)
CRYSOL (closed)	28.2	6.4
FOXS (closed)	28.1	6.3
Custom written (closed)	27.6	6.4
CRYSOL (open)	29.5	4.4
FOXS (open)	29.4	4.4
Custom written (open)	29.4	4.4

Supplementary Figures

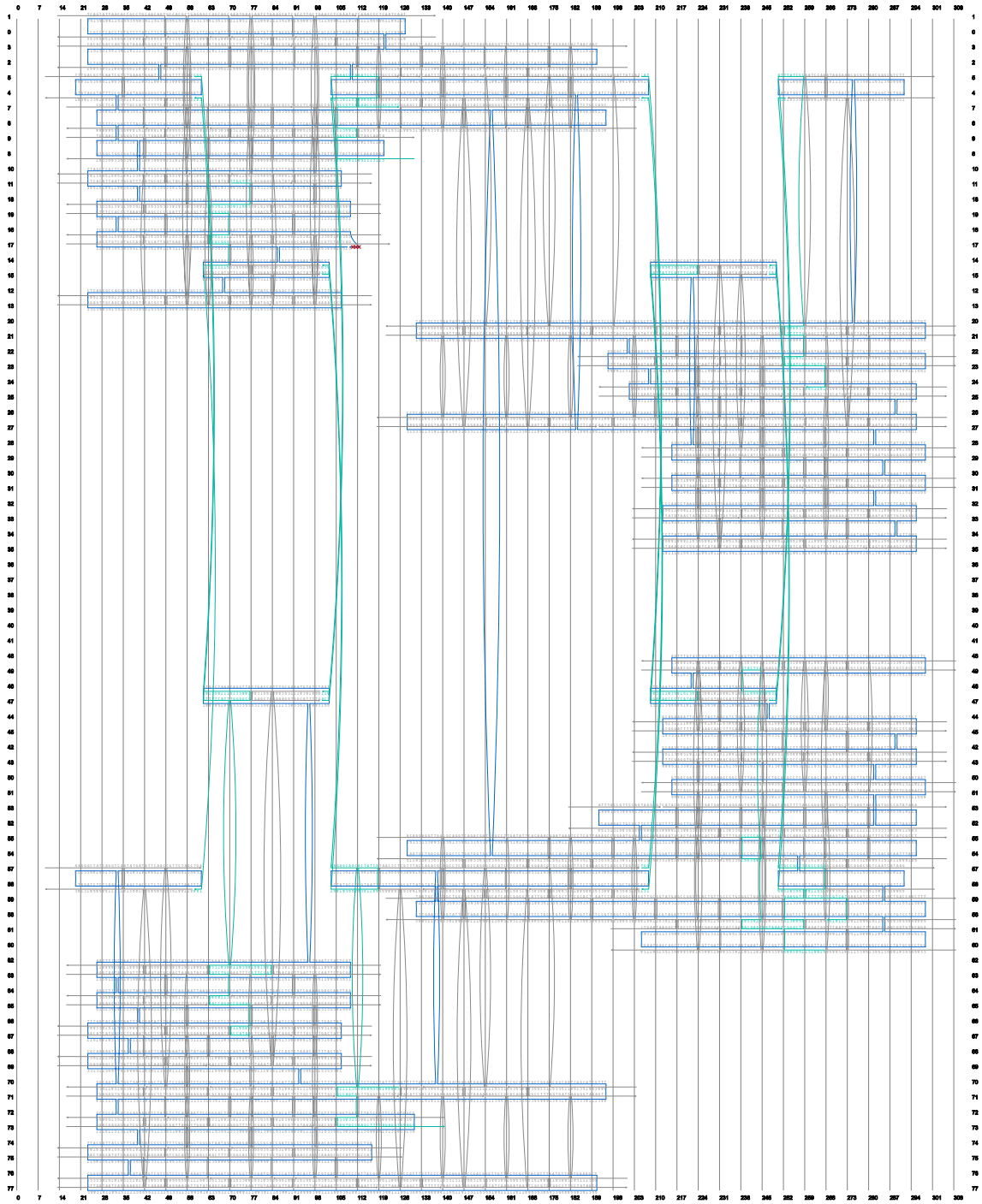

Supplementary Figure S1. Strand diagram of the static closed switch (switch C) variant. Scaffold (shown in blue) and staple layout of the switch C variant. Cyan: 3-bases sticky end. Generated with caDNAno v0.2.

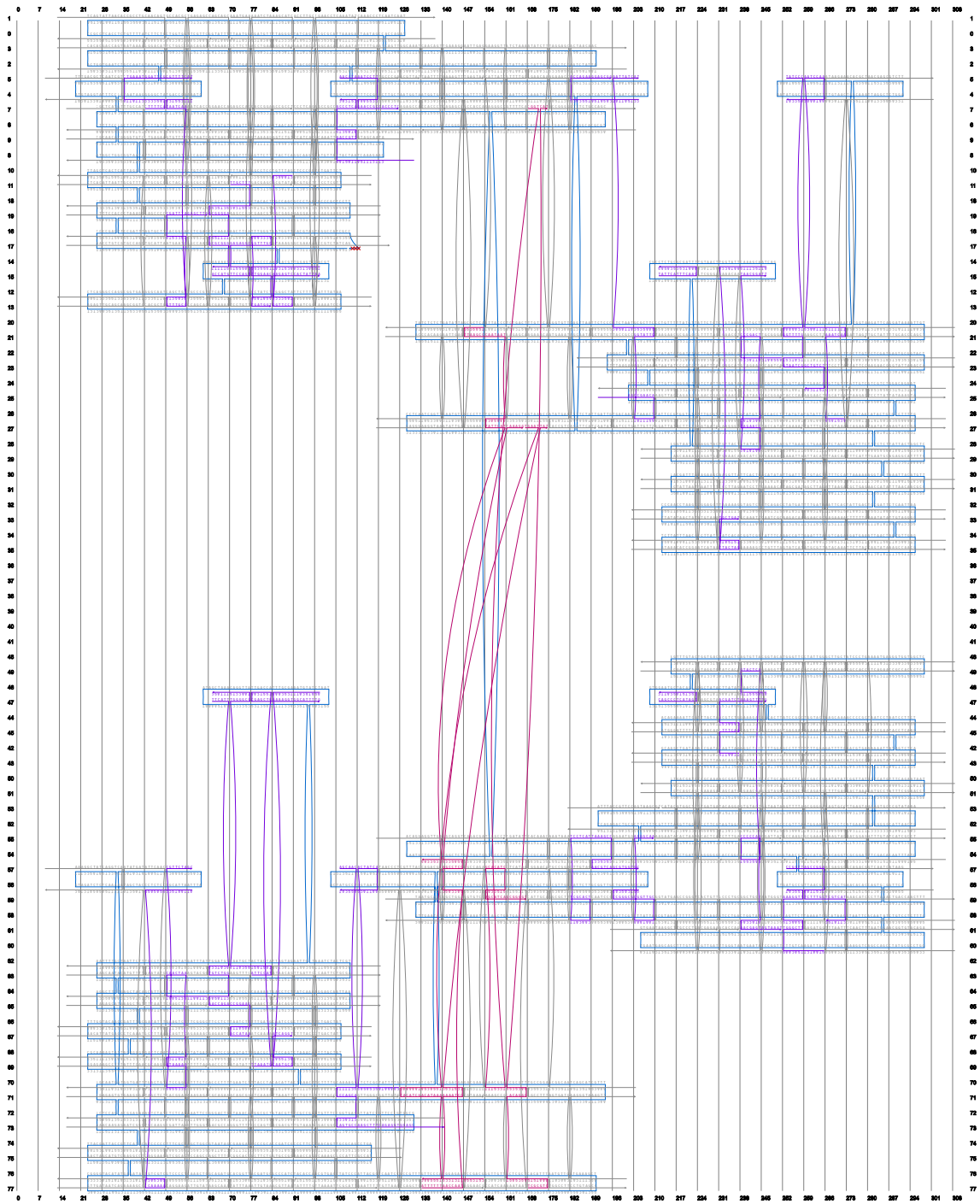

Supplementary Figure S2. Strand diagram of the static open switch (switch O) variant. Scaffold (shown in blue) and staple layout of the switch O variant. Purple: stacking deactivated; Pink: additional connections between the upper and bottom arm. Generated with caDNAno v0.2.

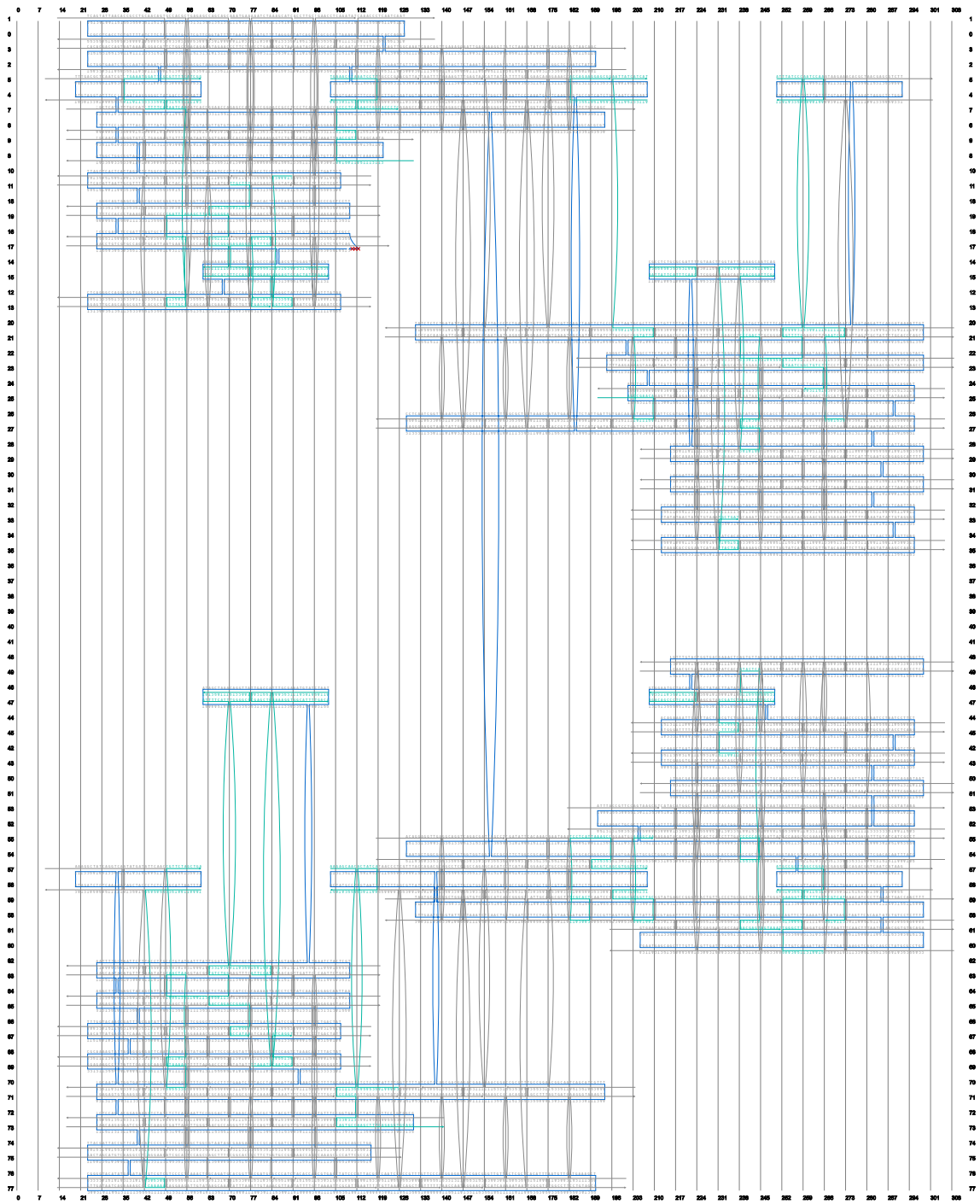

Supplementary Figure S3. Strand diagram of the dynamic (switch D) variant. Scaffold (shown in blue) and staple layout of the dynamic switch variant with 16 activated stacking interactions. Cyan: stacking activated. Generated with caDNAno v0.2.

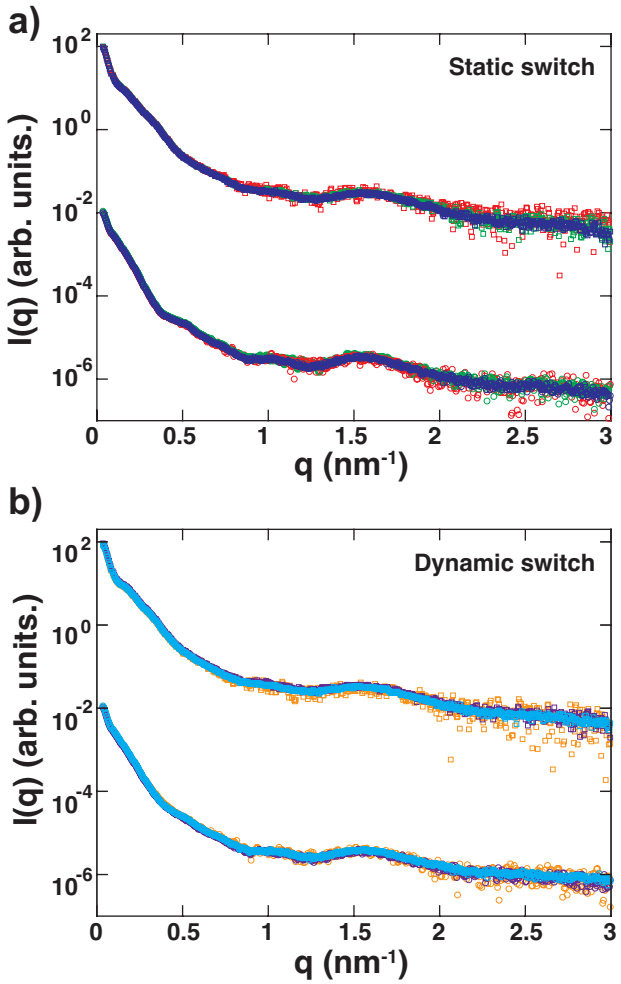

Supplementary Figure S4. Concentration scaled scattering profiles for the static (switch C and switch O, top) and the dynamic (switch D30 and switch D05, bottom) switch variants. (a) Averaged scattering profiles for the switch C (circles, bottom) and switch O (squares, top) measured at varying concentrations: 25 nM (red), 50 nM (green) and 100 nM (blue). (b) Averaged scattering profiles for the switch D30 (circles, bottom) and switch D05 (squares, top) for applied concentrations of 25 nM (orange), 50 nM (purple) and 100 nM (cyan). Profiles are scaled by their concentration and the lower scattering profiles are vertically offset for clarity.

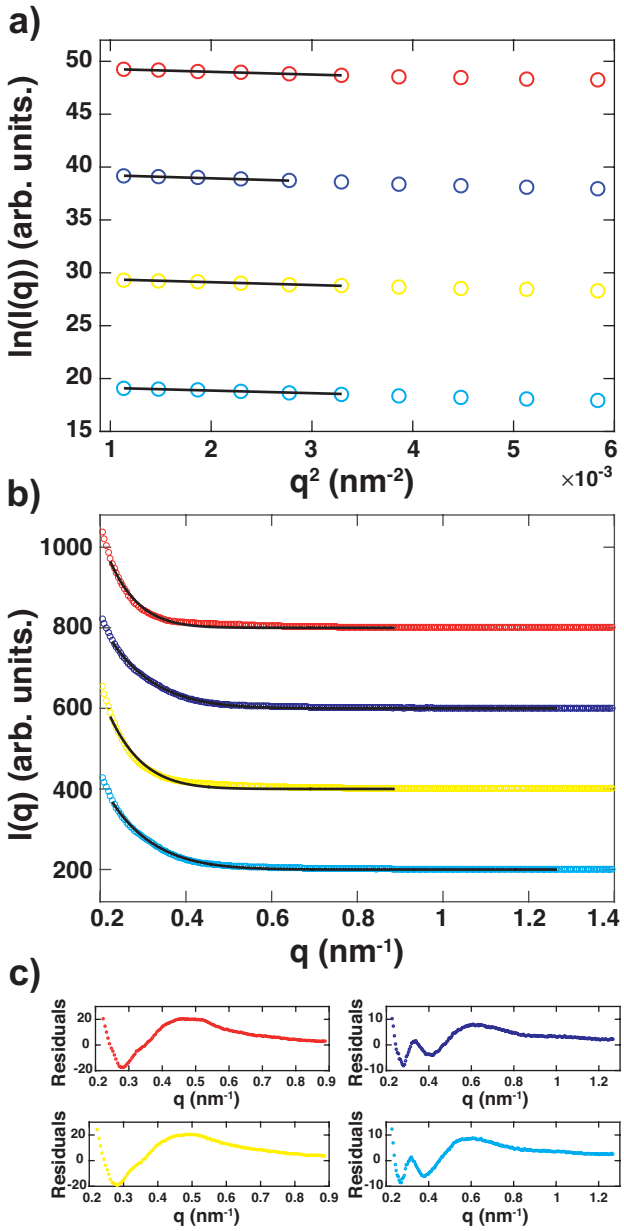

Supplementary Figure S5. Guinier analysis and fits for the cross-sectional scattering intensity of static and dynamic switch samples. (a) Guinier representation of the experimental scattering data for switch C (red, top), switch O (blue), switch D30 (yellow) and switch D05 (cyan, bottom). The Guinier fits are indicated by black lines covering a q-range of $qR_g < 1.6$. Profiles are vertically offset for clarity. (b) Fits of the cross-sectional scattering intensities to experimental data shown in (a) (same color code as in (a)) for the q-range $q_{min} = 2\pi/R_g$ and $q_{max} = 2\pi/R_c$, where the R_c is given by $R_c^2 = R^2/2$. For switch C and switch D30 a radius of R = 10 nm and for switch O and switch D05 a radius of R = 7 nm was assumed for the fit. Profiles are vertically offset for clarity. (c) Residuals for data from (b) (same color code as in (b)).

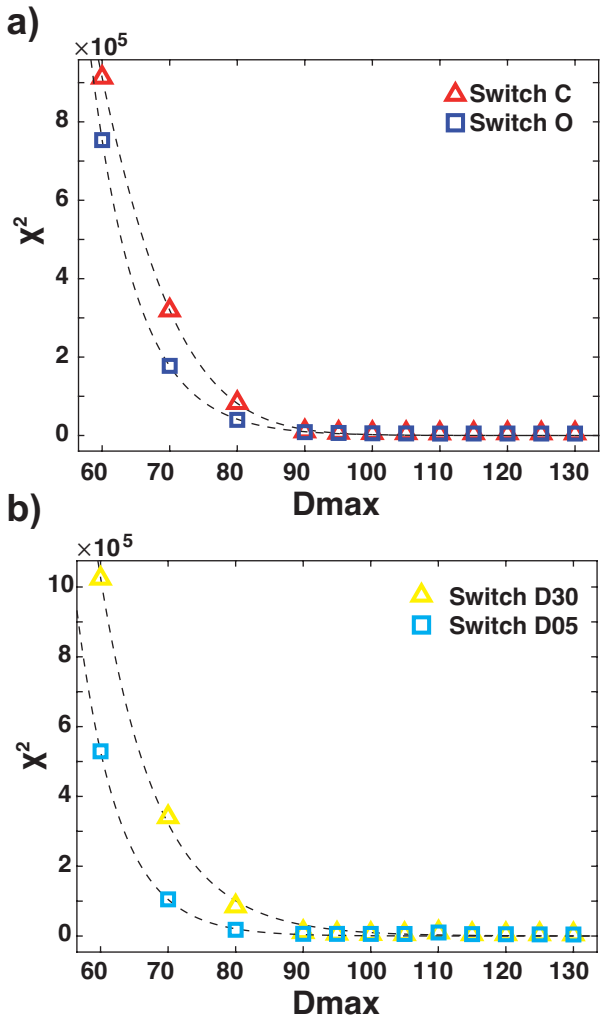

Supplementary Figure S6. Determination of an adequate D_{max} value used for the computation of the pair distance distribution function *P(r)*. (a) χ^2 describing the discrepancy between the experimental data and the fit as a function of different D_{max} values evaluated for the static switch versions switch C and switch O. (b) Corresponding analysis for the dynamic switch versions switch D30 and switch D05. For all samples a mimimun of χ^2 around 95 nm was found, which was applied to calculate the *P(r)* function for each sample.

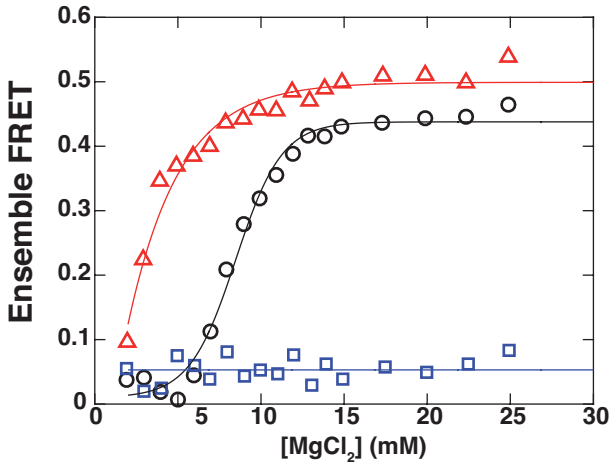

Supplementary Figure S7. Ensemble FRET measured via donor quenching for a titration of $MgCl_2$ in solutions containing switch C (red triangles), switch D (black circles) and the dynamic switch variant with all click contacts deactivated (blue squares). Solid lines represent a two-state model with a free energy term that depends linearly on the $MgCl_2$ concentration (see Equation S9).

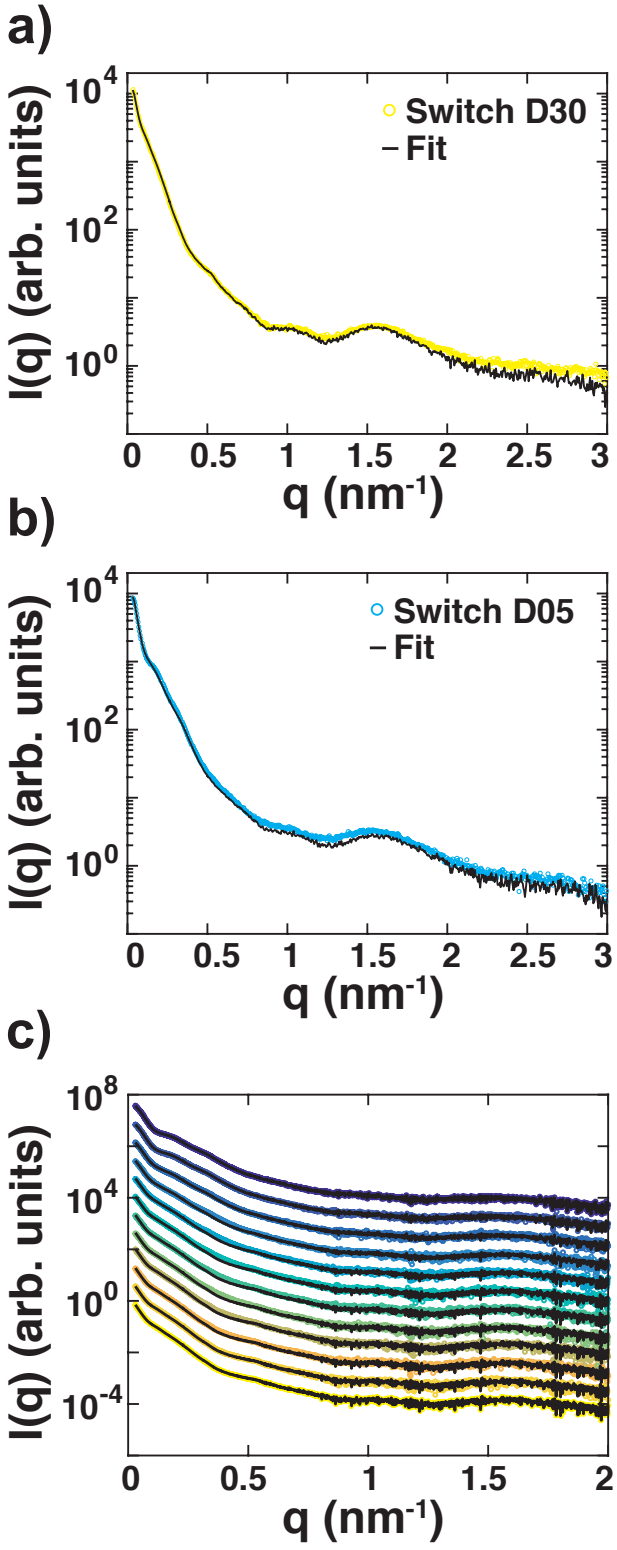

Supplementary Figure S8. Fits of two-state models for the dynamic switch variants (switch D). (a) Scattering profile (yellow) of the switch D30 sample (30 mM $MgCl_2$) and the fitted profile (black) obtained from the two-state model (see main text). (b) Scattering profile (cyan) of the switch D05 sample (5 mM $MgCl_2$) and the fitted profile of the two-state model (black). (c) Scattering profiles of switch D for varying $MgCl_2$ concentrations: 3 (dark blue, bottom), 5, 8, 10, 12, 14, 15, 16, 18, 20, 25 and 30mM (light yellow, top) and fitted profiles from a two-state model (see main text). Data are vertically offset for clarity.

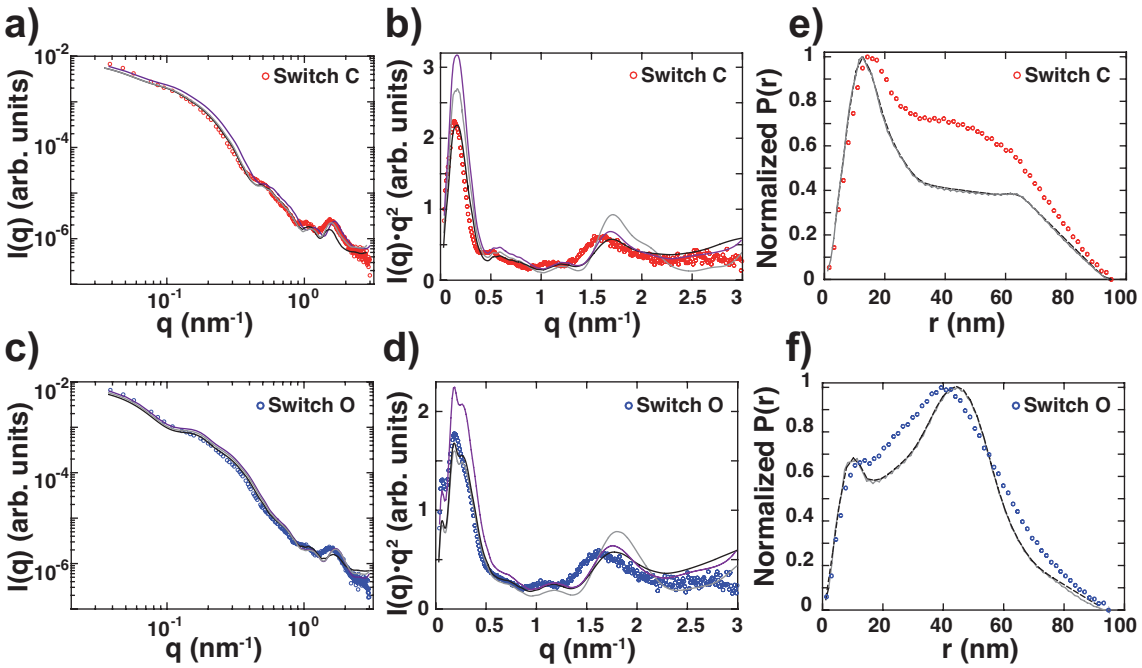

Supplementary Figure S9. Comparison of the experimental and theoretical scattering profiles and P(r) functions that were predicted from the atomistic models derived from CanDo of the static switch samples. (a) Fits including an additional constant in the theoretical scattering profiles calculated with the program *CRYSOL* (black line), *FOXS* (gray line) and a custom written *C* script (purple line) to the experimental data of the switch C sample (red circles). For the custom written routine only one bead per base was assumed. (b) Kratky representation of the data shown in (a) (same color code as in (a)). (c) Fits including an additional constant in the theoretical scattering profiles calculated with the program *CRYSOL*, *FOXS* and a custom written *C* script (same color code and computational settings as in (a)) to the experimental data of the switch O sample (blue circles). (d) Kratky representation of the data shown in (c) (same color code as in (c)). (e,f) P(r) functions of switch C (red circles) and switch O (blue circles) based on experimental scattering data and from profiles derived from *FOXS* (gray line). Black dashed lines correspond to histograms of distances calculated directly from the atomistic models. P(r) data were normalized to unity.

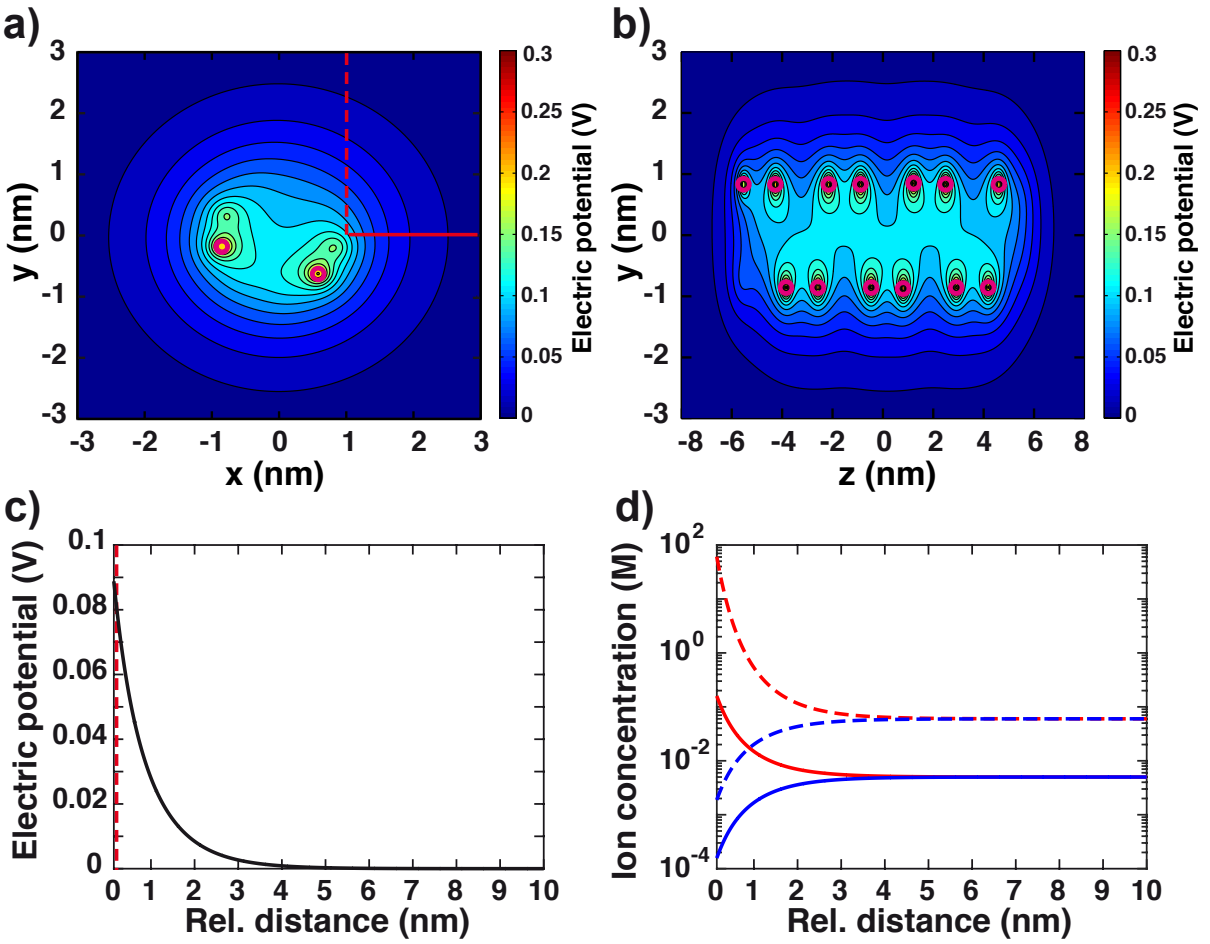

Supplementary Figure S10. Electrostatic potential and ion distribution calculations to estimate the ion atmosphere. (a,b) Contour plots of the screened electrostatic potential for an atomistic model considering only phosphate charges of a 35 bp DNA, showing cross-sections in the x-y plane (a) and y-z plane (b). Magenta circles indicate positions of phosphate atoms. (c) Electric potential along the x-axis (for y,z = 0 nm) corresponding to a solvent-accessible area outside the 35 bp DNA (indicated by the vertical (dashed) and horizontal red lines). (d) Concentration of mono- and divalent ions for the same area as in (c) corresponding to buffer conditions of 5 mM NaCl and 30 mM $MgCl_2$: Mg^{2+} (red dashed line), 2 x Cl^- (blue dashed line), Na^+ (red line) and Cl^- (blue line).

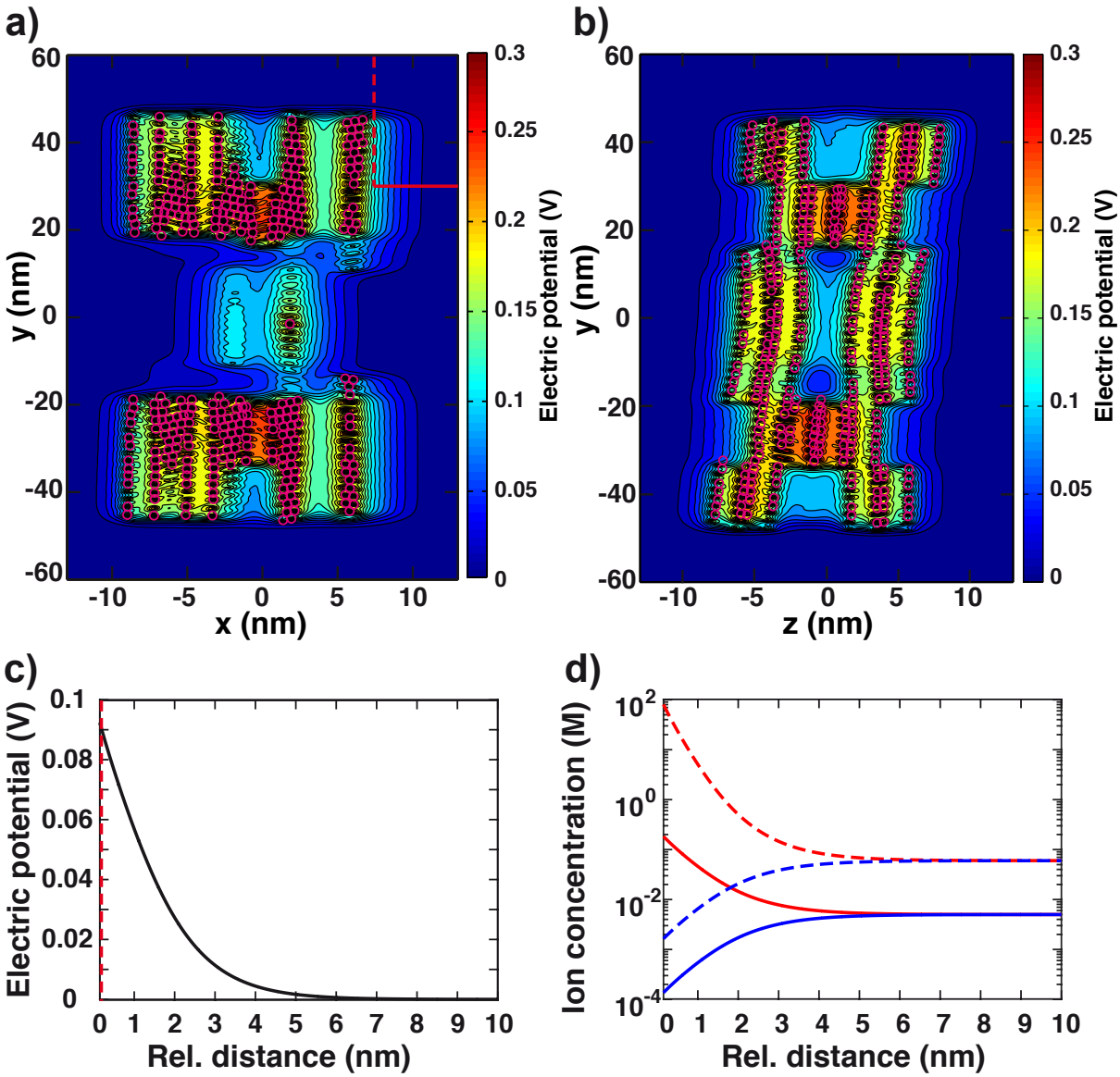

Supplementary Figure S11. Electrostatic potential and ion distribution calculations to estimate the ion atmosphere. (a,b) Contour plots of the screened electrostatic potential for an atomistic model considering only phosphate atoms of switch C, showing cross-sections in the x-y plane (a) and y-z plane (b). Magenta circles indicate positions of phosphate atoms. (c) Electric potential along the x-axis (for y = 30 nm; z = 0 nm) corresponding to a solvent-accessible area outside the switch C structure (indicated by the vertical (dashed) and horizontal red lines). (d) Concentration of mono- and divalent ions for the same area as in (c) corresponding to buffer conditions of 5 mM NaCl and 30 mM $MgCl_2$: Mg^{2+} (red dashed line), 2 x Cl^- (blue dashed line), Na^+ (red line) and Cl^- (blue line).

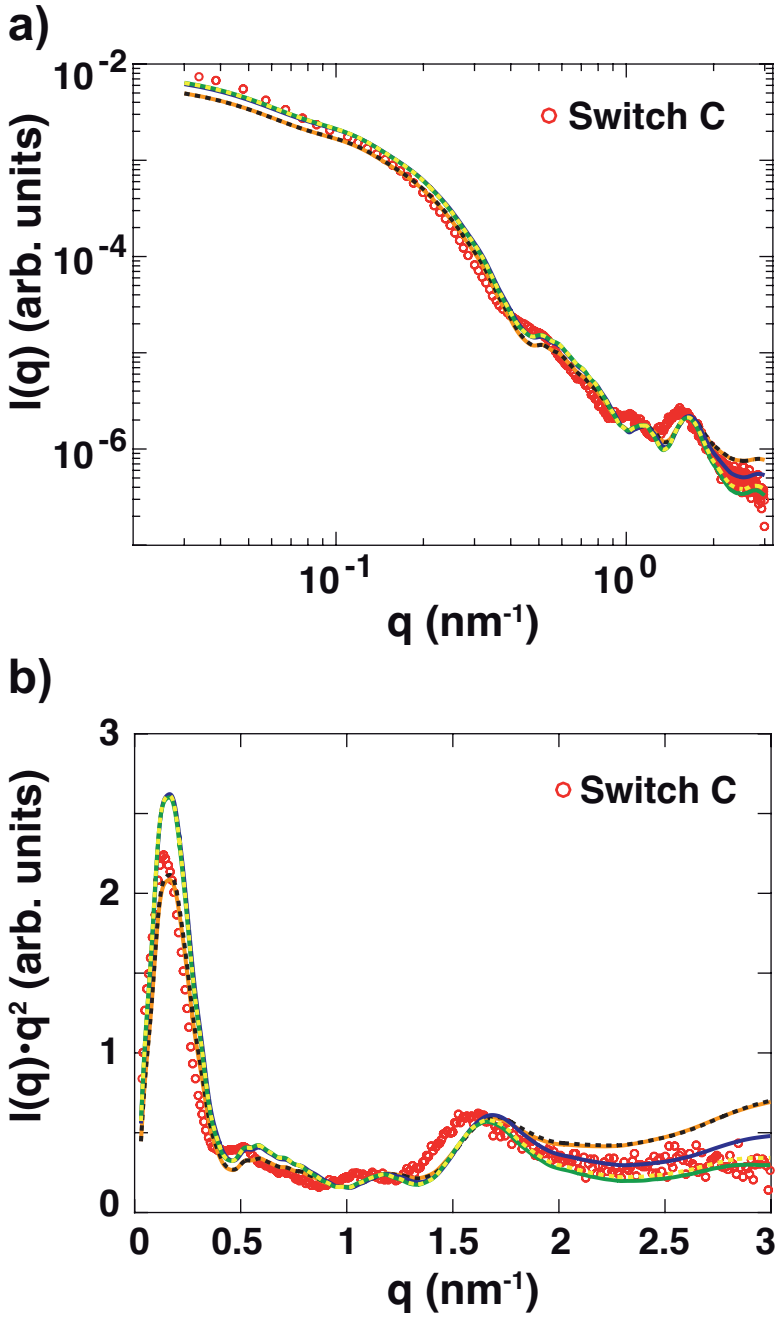

Supplementary Figure S12. Computations of the scattering profiles with varying hydration shell conditions in *CRYSOL*. Linear fits including a constant offset of theoretical scattering profiles calculated with *CRYSOL* with contrast values of the hydration shell of 0.06 e/Å^3 (black dashed line), 0.12 e/Å^3 (orange line) and 0.25 e/Å^3 (green line) (solvent density = 0.334 e/Å^3 for all three profiles), with a solvent density value of 0.344 e/Å^3 and default contrast (blue line) and with a solvent density value of 0.344 e/Å^3 setting the contrast value to 0.25 e/ Å^3 (yellow dashed line). (b) Data from (a) in Kratky representation.

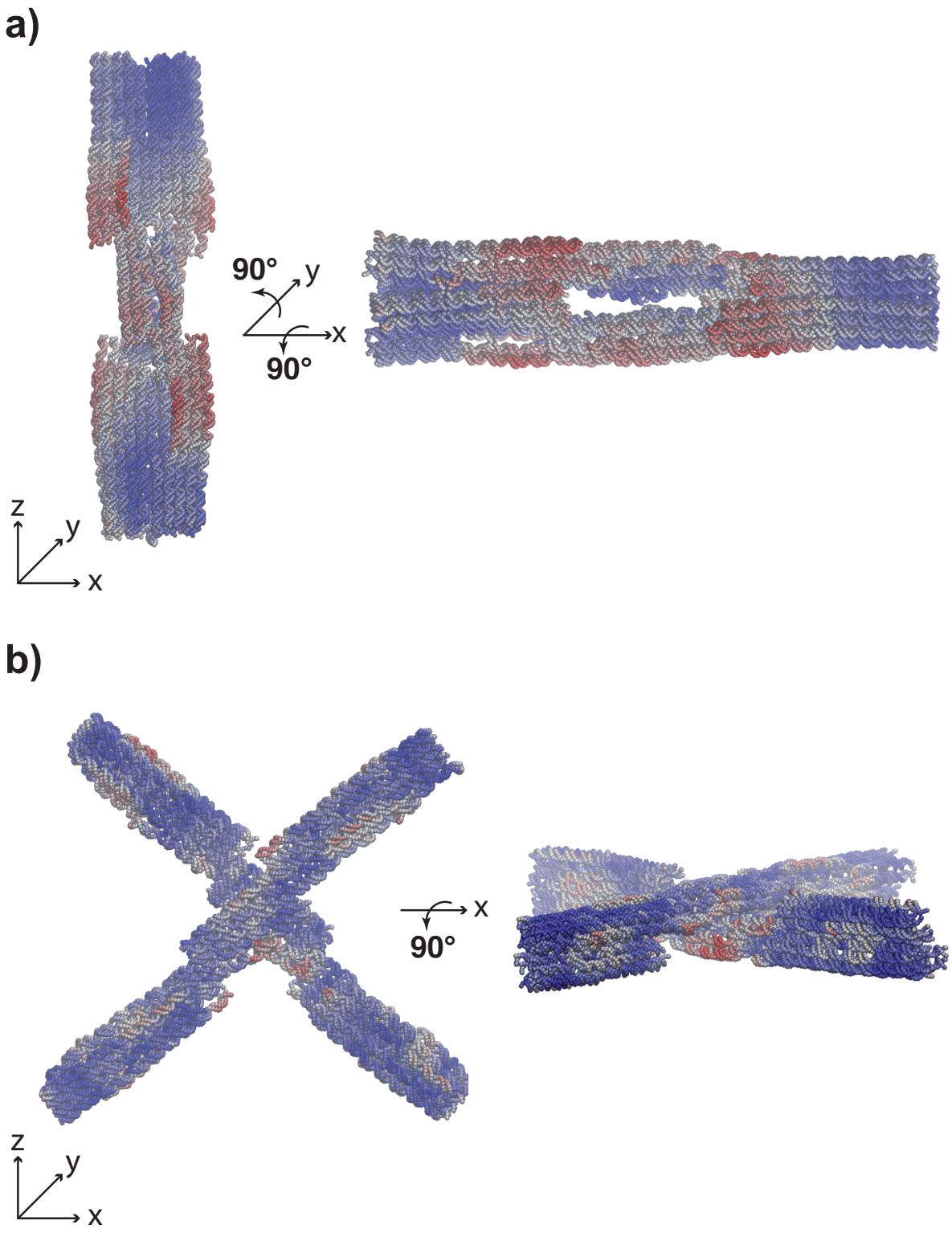

Supplementary Figure S13. Visualization of the switch deformations from the normal mode refinement. (a) Local deformations for switch C (defined as RMSD against the initial CanDo derived structure) are indicated by the colored code where blue and red areas correspond to minimal and maximal deformations, respectively. (b) Local deformations for switch O, same color code as in (a).

Supplementary References

(1) Douglas, S. M.; Marblestone, A. H.; Teerapittayanon, S.; Vazquez, A.; Church, G. M.; Shih, W. M. *Nucl. Acids Res.* **2009**, *37* (15), 5001–5006.

(2) Kick, B.; Praetorius, F.; Dietz, H.; Weuster-Botz, D. *Nano Lett.* **2015**, *15* (7), 4672–4676.

(3) Sobczak, J.-P. J.; Martin, T. G.; Gerling, T.; Dietz, H. *Science* **2012**, *338* (6113), 1458–1461.

(4) Stahl, E.; Martin, T. G.; Praetorius, F.; Dietz, H. *Angewandte Chemie* **2014**, *126* (47), 12949–12954.

(5) Svergun, D. I.; Koch, M. H. J. *Rep. Prog. Phys.* **2003**, *66* (10), 1735–1782.

(6) Lipfert, J.; Herschlag, D.; Doniach, S. *Methods Mol. Biol.* **2009**, *540*, 141–159.

(7) Pernot, P.; Round, A.; Barrett, R.; De Maria Antolinos, A.; Gobbo, A.; Gordon, E.; Huet, J.; Kieffer, J.; Lentini, M.; Mattenet, M.; Morawe, C.; Mueller-Dieckmann, C.; Ohlsson, S.; Schmid, W.; Surr, J.; Theveneau, P.; Zerrad, L.; McSweeney, S. *J Synchrotron Radiat* **2013**, *20* (Pt 4), 660–664.

(8) Blanchet, C. E.; Spilotros, A.; Schwemmer, F.; Graewert, M. A.; Kikhney, A.; Jeffries, C. M.; Franke, D.; Mark, D.; Zengerle, R.; Cipriani, F.; Fiedler, S.; Roessle, M.; Svergun, D. I. *J. Appl. Cryst (2015).* **2015**, 48, 431-443.

(9) Guinier, A. *Ann. Phys. (Paris)* **1939**, 12, 161.

(10) Hammel, M.; Yu, Y.; Mahaney, B. L.; Cai, B.; Ye, R.; Phipps, B. M.; Rambo, R. P.; Hura, G. L.; Pelikan, M.; So, S.; Abolfath, R. M.; Chen, D. J.; Lees-Miller, S. P.; Tainer, J. A. *J. Biol. Chem.* **2010**, *285* (2), 1414–1423.

(11) Kratky, O.; Glatter, O. *Academic Press, London* **1982**, 1–267.

(12) Moore, P. B. *J Appl Crystallogr* **1980**, *13* (2), 168–175.

(13) Shannon, C. E. *Bell System Technical Journal* **2013**, *27* (4), 623–656.

(14) Pan, K.; Kim, D.-N.; Zhang, F.; Adendorff, M. R.; Yan, H.; Bathe, M. *Nature Communications* **2014**, *5*, 5578–7.

(15) Svergun, D.; Barberato, C.; Koch, M. *J Appl Crystallogr* **1995**, *28* (6), 768–773.

(16) Schneidman-Duhovny, D.; Hammel, M.; Sali, A. *Nucl. Acids Res.* **2010**, *38* (Web Server issue), W540–W544.

(17) Schneidman-Duhovny, D.; Hammel, M.; Tainer, J. A.; Sali, A. *Biophys. J.* **2013**, *105* (4), 962–974.

(18) Walther, D.; Cohen, F. E.; Doniach, S. *J Appl Crystallogr* **2000**, *33* (2), 350–363.

(19) Waluyo, I.; Huang, C.; Nordlund, D.; Bergmann, U.; Weiss, T. M.; Pettersson, L. G. M.; Nilsson, A. *J Chem Phys* **2011**, *134* (6).

(20) Meisburger, S. P.; Pabit, S. A.; Pollack, L. *Biophysj* **2015**, *108* (12), 2886–2895.

(21) Andresen, K.; Das, R.; Park, H. Y.; Smith, H.; Kwok, L. W.; Lamb, J. S.; Kirkland, E. J.; Herschlag, D.; Finkelstein, K. D.; Pollack, L. *Phys. Rev. Lett.* **2004**, *93* (24).

(22) Das, R.; Mills, T. T.; Kwok, L. W.; Maskel, G. S.; Millett, I. S.; Doniach, S.; Finkelstein, K. D.; Herschlag, D.; Pollack, L. *Phys. Rev. Lett.* **2003**, *90* (18), 188103.

(23) Pollack, L. *Biopolymers* **2011**, *95* (8), 543–549.

(24) Zheng, W.; Tekpinar, M. *Biophys. J.* **2011**, *101* (12), 2981–2991.

(25) Ravikumar, K. M.; Huang, W.; Yang, S. *The Journal of Chemical Physics* **2013**, *138* (2), 024112–024118.

(26) Gerling, T.; Wagenbauer, K. F.; Neuner, A. M.; Dietz, H. *Science* **2015**, *347* (6229), 1446–1452.